Inter-dot coupling and excitation transfer mechanisms of telecommunication band InAs quantum dots at elevated temperatures

2012 New J. Phys. 14 023037

(http://iopscience.iop.org/1367-2630/14/2/023037)

New Journal of Physics
The open-access journal for physics

Inter-dot coupling and excitation transfer mechanisms of telecommunication band InAs quantum dots at elevated temperatures

C Hermannstädter[1,4], N A Jahan[1,2], J-H Huh[1], H Sasakura[1], K Akahane[3], M Sasaki[3] and I Suemune[1]

[1] Research Institute for Electronic Science, Hokkaido University, Sapporo 001-0021, Japan
[2] Graduate School of Information Science Technology, Hokkaido University, Sapporo 060-0814, Japan
[3] National Institute of Information and Communications Technology, Koganei, Tokyo 184-8795, Japan
E-mail: claus@es.hokudai.ac.jp

New Journal of Physics **14** (2012) 023037 (19pp)
Received 22 November 2011
Published 17 February 2012
Online at http://www.njp.org/
doi:10.1088/1367-2630/14/2/023037

Abstract. We investigate the photoluminescence temperature dependence of individual InAs/InGaAlAs quantum dots emitting in the optical telecommunication bands. The high-density dots are grown on InP substrates and the selection of a smaller dot number is done by the processing of suitable nanometer-sized mesas. Using ensembles of only a few dots inside such mesas, their temperature stability, inter-dot charge transfer, as well as carrier capture and escape mechanisms out of the dots are investigated systematically. This includes the discussion of the dot ensemble and individual dots. Among the single-dot properties, we investigate the transition of emission lines from zero-phonon line to acoustic phonon sideband-dominated line shape with temperature. Moreover, the presence of single recombination lines up to temperatures of about 150 K is demonstrated.

[4] Author to whom any correspondence should be addressed.

Contents

1. Introduction

Solid state semiconductor single-photon emitters, such as self-assembled quantum dots (QDs) [1–3], have recently attracted much attention for a wide range of applications in quantum information and communication [4–8]. They can be used as deterministic photon sources, comparable to single atoms and molecules, impurities in semiconductors, etc. Semiconductor QDs are powerful candidates for single-photon and entangled photon pair generation for applications in state-of-the-art highly secure communication and quantum computation [9, 10]. An operating range in the telecommunication O and C bands (1.3 and 1.55 μm) is favourable to ensure the applicability of standard silica-based fibres and fibre networks. The high photon extraction efficiency of single-QD devices is another significant factor to suppress the bit error rate. The inter-dot coupling [11–17] as well as the interaction of the QDs and the confined carriers with their environment are important phenomena either to exploit them to manipulate the quantum state [18, 19] or to suppress them in order to keep the QD of interest as isolated as desired. A detailed understanding and description of these interactions gains importance when the system temperature is increased above liquid helium temperature (4.2 K) and towards technically more easily achievable temperatures above liquid nitrogen temperature (77 K), because thermally activated processes come into play.

We realized metal-embedded tapered mesa (nano-cone) structures to meet the challenge of studying a low number of QDs in the telecommunication O and C bands and to provide low-loss photon extraction, in a comparable approach to the demonstration by Takemoto *et al* [20]. The advantages of the proposed and realized nano-cones are their fast and highly reproducible nanometer- (or micrometer-)sized fabrication, the possibility to integrate them in more complex devices and the efficient light extraction by embedding them inside reflective metal. In this paper, we briefly discuss the nano-cone structure fabrication process with the main purpose of isolating individual dots and creating nanostructures of efficient photon extraction. The excitons confined to individual QDs as well as their relaxation and recombination are investigated in detail with a focus on their temperature dependence. The thermally induced exciton transfer between and escape from QDs is described using a simple model. The optical spectroscopy results, furthermore, present wavelength-tunable/selectable single QD emission towards the realization of a practical single-photon source in both the telecommunication O and C bands.

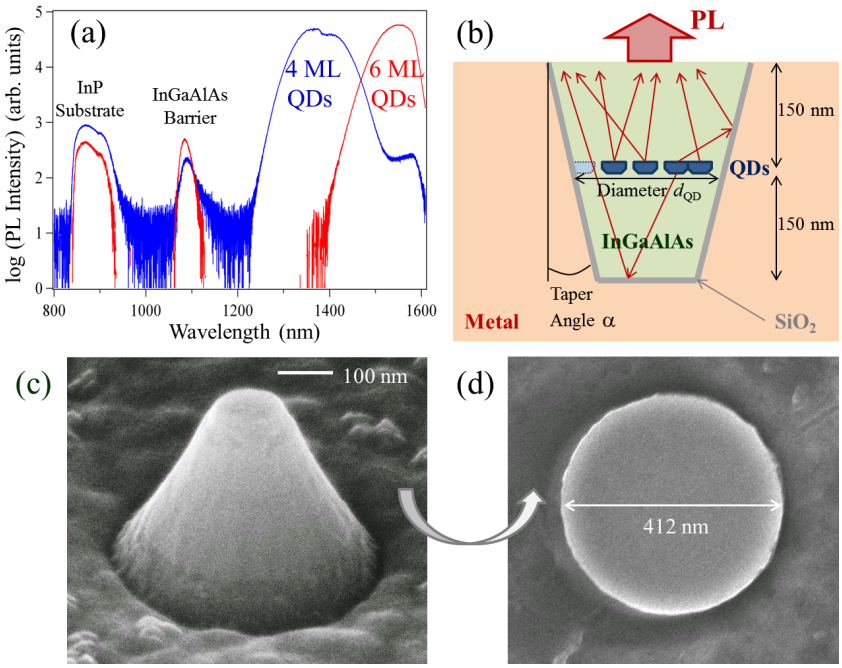

Figure 1. (a) PL of the 4 and 6 ML InAs QD samples at 10 K, including the emission from the InP substrate and the $In_{0.53}Ga_{0.22}Al_{0.25}As$ barrier. (b) Schematic illustration of the PL structure, a metal-embedded cone, with a thin insulator layer (SiO_2/Si_3N_4) between the metal and the semiconductor part and the QDs located in the center of the InGaAlAs barrier. (c) Side view SEM image of an as etched 26° tapered nano-cone with a tip diameter of about 100 nm and a diameter of the QD-containing plane of $d_{QD} \approx 250$ nm; (d) top-view SEM image of the respective turned-around and SiO_2/Ti-embedded nano-cone with removed substrate.

2. Samples and experiment

The investigated samples contain high-density ($\sim 1 \times 10^{11}$ cm^{-2}) InAs QDs grown on a lattice matched 150 nm thick $In_{0.53}Ga_{0.22}Al_{0.25}As$ buffer layer on InP(311)B substrates by molecular beam epitaxy [21, 22]. For optical measurements the QDs were capped with another 150 nm thick $In_{0.53}Ga_{0.22}Al_{0.25}As$ barrier layer. QD emission between 1.2 and 1.6 μm (1.03–0.77 eV) could be achieved by varying the nominal thickness of the optically active QD layer between four and six monolayers (MLs); the photoluminescence (PL) of these as grown, unstructured samples is displayed in figure 1(a). These QD samples have no wetting layer, which can be concluded from the PL spectra, where no indication for the respective luminescence is found[5]. The absence of a wetting layer has vast consequences for the QD optical properties and charge redistribution processes, which will be discussed in the following sections. Sequential steps of electron-beam lithography and etching allowed for a well-controlled and high-yield fabrication of nano-cones with typical 26° taper angles, heights of 300 nm and tip diameters down to less

[5] The referred experimental data were obtained from an unstructured sample containing the exact same InAs QDs (same epitaxy) as are discussed in this paper [23].

than 100 nm (figures 1(b) and (c)). After the deposition of a thin insulating layer (10–60 nm SiO_2 or Si_3N_4), the nano-cones were embedded in metal (titanium (Ti) or silver (Ag)). In the subsequent step, the InP substrate was removed and the sample was turned upside down, which is highlighted in the schematic illustration and top-view scanning electron microscope (SEM) image in figures 1(b) and (d) (more details of the fabrication are presented in [24]). In the further text the diameter of the QD-containing plane, d_{QD}, of the nano-cones is given when nano-cone sizes are specified.

The PL of such turned-around and metal-embedded nano-cones was investigated in a micro-PL setup optimized for the near-infrared (NIR) spectral range. The samples were cooled in a helium-flow cryostat to access a temperature range from 4 K to room temperature. For non-resonant excitation a HeNe laser (632.8 nm; 1.959 eV) was focused on the sample using an NIR-coated NA = 0.42 objective lens, which results in a spot size of approximately 1.5 μm. The PL was collected with the same objective lens and dispersed by a 50 cm double monochromator with 300 grooves per mm gratings and detected by a liquid-nitrogen-cooled InGaAs-photodiode array detector (cutoff $\approx$ 1.6 μm).

3. Quantum dot (QD) luminescence at about 1.3 μm

In this section, the focus of the experimental results and the following discussion is based on the smaller 4 ML QDs which have their low-temperature PL centred at about 1.3 μm (0.95 eV). Using these QDs the temperature dependence up to the complete quenching can be investigated within the sensitivity range of our detector. The PL wavelength furthermore coincides with the telecommunication O band.

3.1. QD photoluminescence power and temperature dependence

The complete PL spectrum from a nano-cone ($d_{QD} \approx 250$ nm) is displayed in figure 2(a), where at low excitation power a total of about ten optically active QDs are visible between about 0.88 and 1.02 eV. With increasing excitation power additional PL lines at higher energy emerge which are due to excited state recombination in the QDs. At the highest excitation power, the InGaAlAs barrier luminescence can be seen at about 1.180 eV; no wetting layer exists for this type of QD sample. For the first 4 ML QD, which is shown on the left side of the more detailed close-up, figures 2(b) and (c), X0 and X* exhibit an almost linear dependence ($S \approx 0.9$) of their intensities, I, on excitation power, P_{Exc}, in the respective power law, $I \propto P_{Exc}^{S}$. This indicates their origin from neutral and (negatively) charged exciton recombination. XX shows a super-linear dependence ($S \approx 1.35$) indicating its origin from biexciton recombination. The second presented dot on the right side of the close-up, figures 2(b) and (d), does not show the same clear power dependence; however, X1 and X3 depend slightly super-linearly on the excitation power, whereas X2 and X4 exhibit a sub-linear power dependence. Given the relative peak energies and the power dependences, X1 ($S \approx 1.17$) might be due to a charged biexciton or a positive trion and X3 ($S \approx 1.05$) due to a neutral biexciton. The other two peaks are likely assigned as follows: X2 ($S \approx 0.72$) to a neutral exciton and X4 ($S \approx 0.72$) to a (negative) trion. In the following discussion, the exact origin of the recombination lines is not further discussed and is not of major importance.

The PL of the same nano-cone with all contained optically active QDs was examined depending on the excitation power and as a function of the sample temperature between

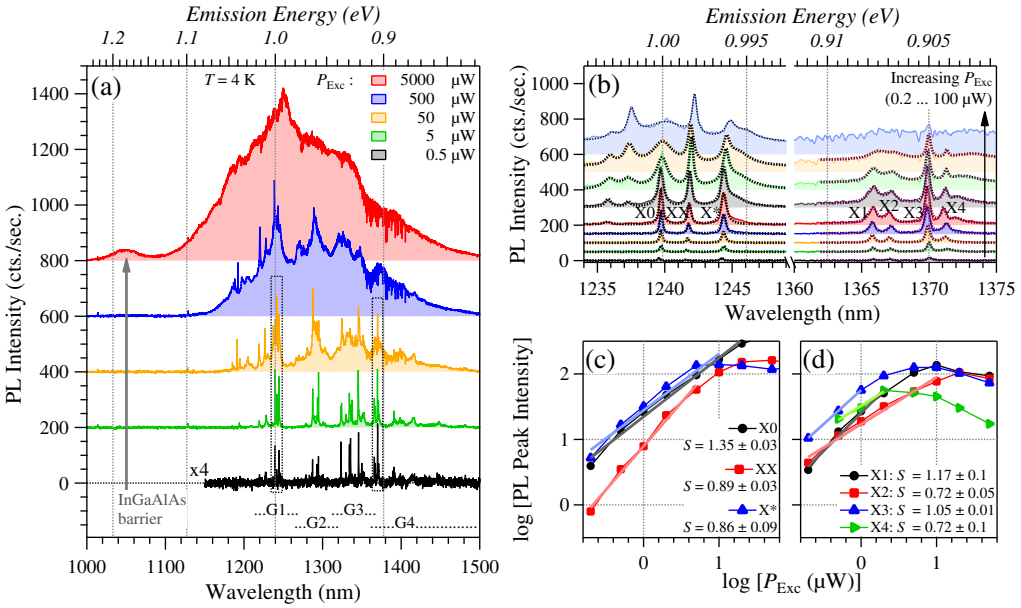

Figure 2. (a) PL power dependence of a $d_{QD} \approx 250$ nm SiO_2/Ti-embedded nano-cone under non-resonant excitation at 4 K. Four groups (G1–G4) of QD emission lines are indicated according to their spectral position for later identification. (b, c) Three PL lines of a single QD at about 1 eV and (b, d) four PL lines at about 0.905 eV at different excitation powers. The power-dependent integrated PL peak intensities are fitted with a power law ($I \propto P_{Exc}^{S}$).

10 and 160 K. The spectra obtained under low, medium and high (above exciton saturation) power conditions are displayed in figure 3. All three presented data sets, (a–c), are comparable, i.e. their scalings and relative offsets are chosen identically; only the lowest-power data (a) are displayed on half the intensity scale and thus with half the offsets for more clarity. Comparing the PL temperature dependence for the different excitation regimes, the first obvious observation is that for higher-power excitation the PL quenching seems much less pronounced, i.e. the PL persists up to higher temperatures. This might be intuitively attributed to refilling processes that take place under non-resonant excitation, where the carriers can repopulate the QDs, which leads to a 'slower' quenching of all dots. Another rather obvious qualitative observation is the emergence of excited states, which results in a major modification of the PL temperature dependence in the high-power case (figure 3(c)). More detailed examination, analysis and discussion of the temperature dependence of both the complete nano-cone PL (QD ensemble) and individual QD PL (single QDs) are carried out in the following section.

3.2. Analysis and discussion

The temperature-dependent PL is analysed by fitting with a model that accounts for both the carrier capture and the quenching temperature dependence,

$$I(T) = I_0 \left(p + \frac{1-p}{\exp[k_B T_0/(k_B T)]} \right) \times \frac{1}{1 + \sum_{i=1,2} b_i \exp\left[-E^{(ai)}/(k_B T)\right]}. \quad (1)$$

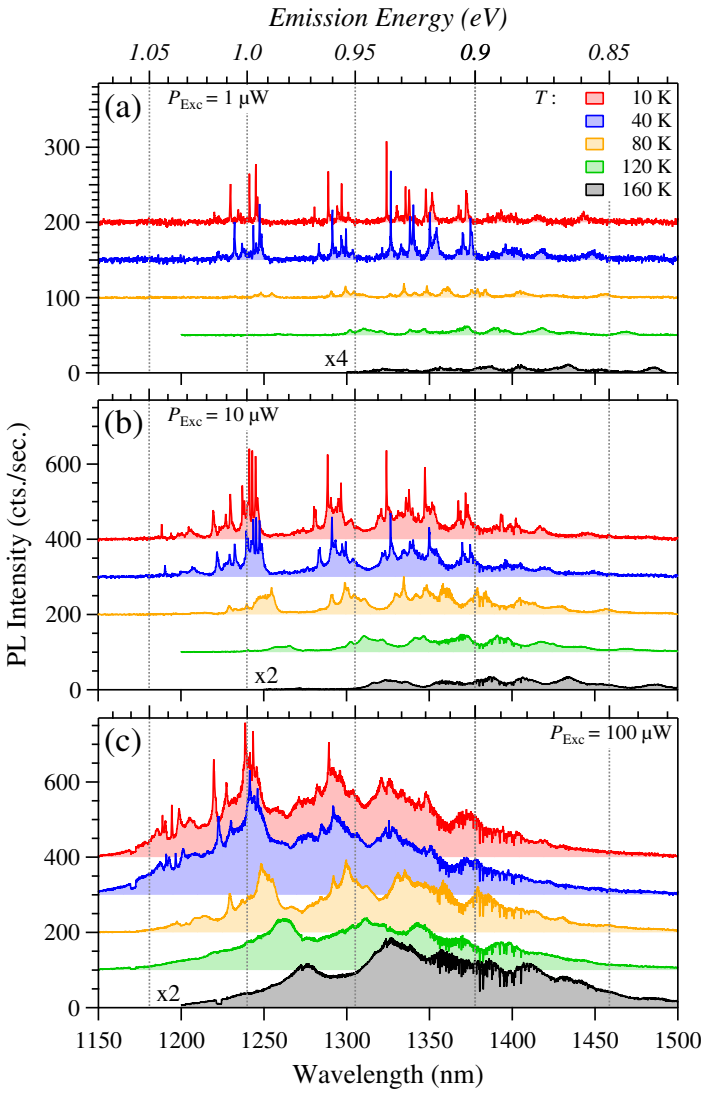

Figure 3. PL temperature dependence from the same nano-cone shown in figure 2 between 10 and 160 K for three different excitation conditions: (a) low-power (1 μW, well below exciton saturation), (b) medium-power (10 μW, approaching saturation), and (c) high-power (100 μW, above saturation) non-resonant excitation.

Therein, the first factor describes the temperature-dependent excitation (carrier capture) that takes place under non-resonant excitation and the second factor describes the thermal quenching of the states for increasing temperatures [25], which includes two distinct escape mechanisms labelled with the index $i = 1, 2$. The parameters in the excitation term are the total (maximum) intensity I_0, the dimensionless weighting parameter p, which defines the ratio between temperature-independent and temperature-dependent excitation contributions, and the temperature constant T_0, which defines a temperature equivalent for the excitation process; k_B is the Boltzmann constant and T is the system temperature. In the quenching term, $E^{(ai)}$ are activation energies that are assigned to a certain escape mechanism and b_i are the corresponding

Table 1. Fit parameters (equation (1)) for the integrated PL from the nano-cone, i.e. from the contained QD sub-ensemble; the 1σ-fit-errors are omitted when not of significant magnitude ($\ll 1\%$ of the parameter value).

$P_{\mathrm{Exc}}(\mu\mathrm{W})$	I_0	p	T_0 (K)	b_1	$E^{(a1)}$ (meV)	b_2	$E^{(a2)}$ (meV)
100	2.2×10^5	0.0084	129 ± 1	184 ± 1	13.0 ± 0.1	$1.4 \times 10^4 \pm 0.02 \times 10^4$	73 ± 1
10	1.0×10^5	0.0055	175 ± 3	410 ± 6	18.4 ± 0.3	$3.6 \times 10^6 \pm 0.2 \times 10^6$	135 ± 6
1	5.5×10^4	0.0014	166 ± 6	1058 ± 73	18.0 ± 0.8	$5.4 \times 10^7 \pm 1.1 \times 10^7$	139 ± 23

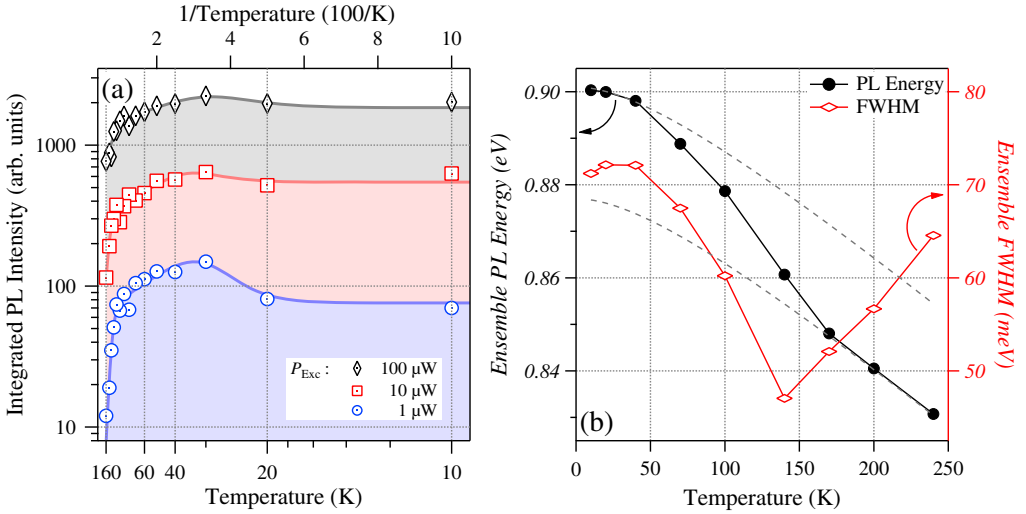

Figure 4. (a) Temperature dependence of the integrated PL of the complete spectra displayed in figure 3 for low, medium and high excitation powers (markers) and the respective fits with equation (1) (filled solid lines). (b) Temperature dependence of the ensemble PL data acquired from an unstructured QD sample for comparison [23]; the emission energy of the ensemble (black circles, obtained from Gaussian line fits), with the dashed grey guide lines obtained from fitting the low- and high-temperature data by the Varshni empirical equation ($E(T) = E_0 - (a/T^2)/(b+T)$), and the ensemble PL full-width at half-maximum (FWHM) (red diamonds).

dimensionless fitting coefficients. The meaning of these coefficients b_i can be understood as the ratio of escape and capture rates of the described mechanism, i.e. $b_i \propto (\text{escape rate})_i/(\text{capture rate})_i$, as is discussed and derived in a comprehensive fashion by Le Ru *et al* in [26].

We start with a comprehensive analysis of the ensemble PL of all QDs within the investigated nano-cone, which is later referred to as QD sub-ensemble. This is done by integration of the total PL intensities within the spectral range displayed in figure 3. The obtained integrated intensities for the three different excitation powers are displayed as a function of inverse temperature in figure 4(a). The decision to display the inverse temperature dependence has been made to show the low-temperature side in a more distinctive way. This addresses the fact that especially the carrier capture (and also re-excitation) processes are heavily dependent on the power regime. The experimental data were fitted using the afore-introduced equation (1) and all obtained fitting parameters are summarized in table 1.

On the excitation side, it is obvious that in the case that the excitation power remains below the exciton saturation, i.e. for 1 μW (blue circles) and 10 μW (red squares), the carrier capture process is rather inefficient, which is revealed by the large obtained characteristic temperature $T_0 \approx 170$ K and the small values of the corresponding constant $p \approx 0.0014$ and 0.0055. The increase in PL intensity up to 30 K in the respective data sets highlights this behaviour. With increasing excitation power, the carrier capture process becomes more efficient or, in other words, less temperature sensitive, indicated by increasing values of p and decreasing values of T_0. This trend is highlighted by the flattening of the data on the low-temperature side with increasing excitation power. For high-power excitation above the exciton saturation (100 μW, black diamonds), also T_0 significantly decreases to 129 K and p further increases.

On the decay side, the following trend can be seen. For both the low- and medium-power excitation regimes, which have no significant contribution of excited states, very similar behaviour is observed. This includes the two different escape mechanisms with activation energies of $E^{(a1)} \approx 18$ meV and $E^{(a2)} \approx 140$ meV, respectively, which are almost the same for the low- and medium-power conditions. For the high-power case, in contrast, especially the larger activation energy becomes significantly smaller, $E^{(a2)} \approx 73$ meV. We assign the first mechanism, $i = 1$, to a process unique for high-density QD ensembles, which is related to inter-dot coupling [11], and the second mechanism, $i = 2$, to the thermal carrier escape from QDs to the barrier.

The discussion of the second mechanism, which leads to significantly reduced activation energy at high excitation power, directly explains the impact of the populated excited states and can be understood rather straightforwardly and intuitively. The carrier escape is directly related to non-radiative carrier escape to the InGaAlAs barrier, which embeds the QDs, and leads to a linear relation between the barrier-dot energy separation and the activation energy $E^{(a2)}$. The energy separation between the barrier and the QD excited states (no matter what kind of states they are) is significantly lower than for the QD ground states, and thus their enhanced population at higher excitation rates leads to a reduction of the corresponding activation energy $E^{(a2)}$. The accompanying fact that also b_2 is smallest at high excitation power supports the aforementioned occurrence of re-excitation, as it indicates a larger corresponding carrier (re-)capture rate. More details, including a quantitative discussion and explanation of the activation energy magnitudes, are presented for single QDs in section 3.2.2.

The first escape mechanism, however, needs a more in-depth description, which is provided by taking a closer look at an ensemble of the same type of QDs (figure 4(b)). For this reference measurement, an unstructured sample and a macroscopic PL setup were used in order to simultaneously access a larger number of QDs for a better statistical distribution and thus ensemble average [23]. The temperature dependence of a QD ensemble under low-power excitation conditions indicates that, firstly, the peak emission energy exhibits a pronounced shift to lower energies when compared to the expected trend using a fit by the Varshni empirical equation and, secondly, the PL ensemble line width decreases with increasing temperature up to about 140 K. These observations can be well explained by a charge–carrier redistribution from the higher- to the lower-energy dots of the ensemble, which is promoted by an increased temperature and thus enhanced phonon scattering and thermal excitation. In order to conclude a corresponding carrier escape process from these rather obvious facts, we suggest to introduce coupled excited states (CES) which are delocalized over many (or even all) dots of the sub-ensemble. When carriers are excited to such a delocalized state, they can either relax favourably to the lowest-energy states, which results in the redistribution in favour

of the lower-energy dots, or be subsequently further excited to the barrier and thus escape the QDs. This process is also discussed in more detail for individual QDs in section 3.2.2, where the relative change of intensities and the change of related activation energies allow for much better insight. To apply this mechanism on the herein described QD sub-ensemble, it shall only be added that for all excitation conditions such small activation energies to a CES could be obtained ($E^{(a1)} \approx$13–18 meV). Moreover, with increasing power, the corresponding b_1 parameter decreased, which again indicates an enhancement of the corresponding (re-)capture-rate, i.e. the relaxation from CES to a QD ground state.

We want to add that in contrast to typical self-assembled InAs/GaAs QDs, remarkably similar behaviour for ensembles of high-density InAs/GaAs quantum posts has been reported [27–29]. This includes both the intensity increase and the charge redistribution from higher- to lower-energy states with increasing temperature. In analogy to our QDs discussed in this paper, also these quantum posts are not coupled to a wetting layer rather than to a surrounding matrix-quantum well as illustrated in [29].

3.2.1. Single-QD spectral properties. In the next step, we investigate the temperature dependent phenomena within the nano-cone in a more detailed way and from a microscopic viewpoint with the aim of describing what happens on the single-QD level and what promotes the inter-dot coupling. Therefore, we take another and closer look at the temperature dependence of the nano-cone PL under low excitation power, which is represented by the detailed dataset displayed in figure 5. This in-depth analysis includes multi-peak fits to all featured QD PL lines, accounting for changing line shapes and emission energies with increasing temperature.

The behaviour of a single PL line, 'Peak 3', is illustrated in figure 6. The zero-phonon line (ZPL), which is represented by the Lorentzian component with an initial line width of 0.17 meV, dominates the spectral shape at low temperatures and initially gains intensity for $T \leqslant 30$ K and then starts to fade for $T > 30$ K. At about 50–70 K, the acoustic phonon sidebands, represented by the Gaussian component, exhibit comparable intensities [30]. In addition to acoustic phonon broadening, also charge fluctuations and contributions of additional capture and decay processes related to QD coupling and higher energy phonons might contribute to this broadening for increasing temperatures. The transition regime is highlighted for 60 K as the inset in figure 6(a), featuring the two distinct components, the ZPL (solid black line) and the phonon sidebands (dashed grey line). For $T > 80$ K the phonon sideband intensity decreases slowly, while the ZPL rapidly diminishes and eventually vanishes completely at about 120 K (figure 6(b)). This particular recombination line can at least be identified as a single PL peak up to about 100 K without significant background or overlap from other features. Although it remains visible for temperatures up to 160 K, eventually background and overlapping of different features become more significant for $T \geqslant 120$ K (figure 5).

The initial intensity increase up to 30 K can be explained, as before, by a not perfectly efficient carrier capture from the barrier to the QD under low-power non-resonant excitation. The temperature dependence of the initial carrier capture is again included in the quantitative discussion and modelling of the individual QD temperature dependence, which follows in section 3.2.2. The relative total line width broadening can be assigned to the two main contributions that are highlighted in figure 6(c): the broadening of the ZPL, which will be discussed later, and the change in relative weight between the narrower ZPL and the broader acoustic phonon sidebands with increasing temperature.

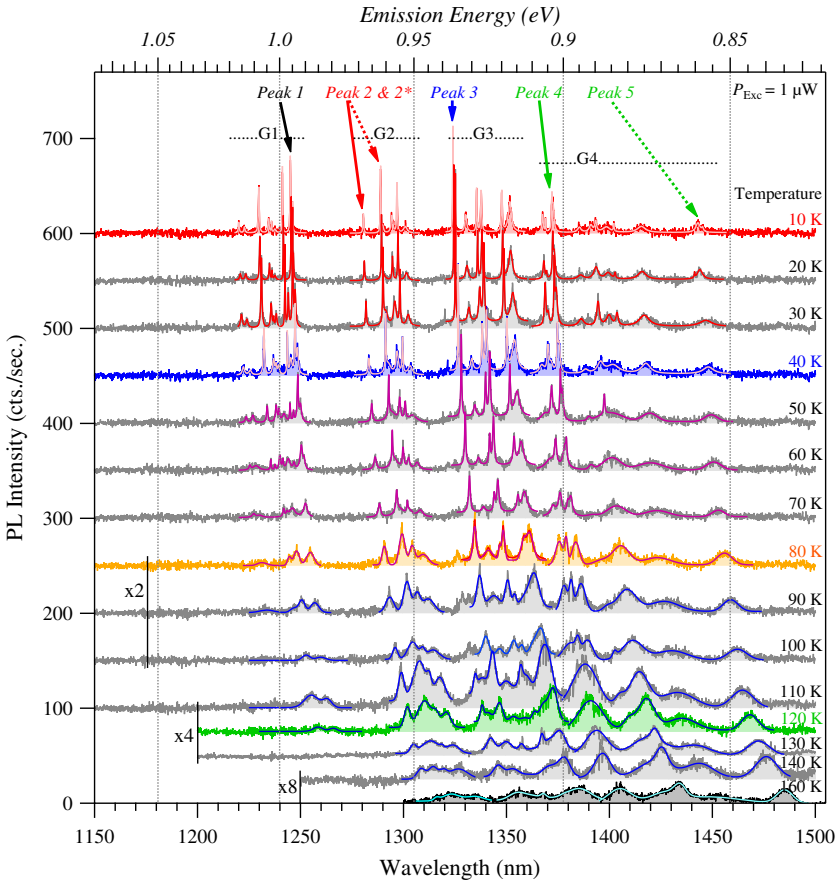

Figure 5. Detailed temperature series (10–160 K) under low-power non-resonant excitation and line fits to all QD spectra. The PL lines, '*Peaks 1–5*', are highlighted for later identification. The data and respective line colours at 10, 40, 80, 120 and 160 K are the same as shown in figure 3(a). The line fitting was obtained using quasi-Voigt functions and using a superposition of Lorentzian and Gaussian functions with changing weight for increasing temperatures (details in figure 6).

In the following paragraph, the temperature dependence of individual QD emission, exemplified by the four PL lines highlighted as 'Peaks 1–4' in figure 5, is analysed using phonon–carrier coupling. The respective emission energy and line width data as well as the corresponding fits are summarized in figure 7. Firstly, we discuss the change in the QD PL emission energies with increasing temperature (figure 7(a)). Assuming phonon–carrier coupling as the most relevant mechanism leads to an empirical fit function based on a Bose–Einstein statistical factor with an average phonon energy, $\langle E_{\mathrm{ph}}^{\mathrm{E}} \rangle$, which causes the energy shift, as introduced, e.g., in [31] (among various others),

$$E(T) = E_0 - \frac{S_{\mathrm{c}}}{\exp[\langle E_{\mathrm{ph}}^{\mathrm{E}} \rangle / (k_{\mathrm{B}} T)] - 1}. \tag{2}$$

E_0 is the zero-temperature energy and S_{c} is the constant describing the strength of the electron–phonon coupling. Since the fitted average phonon energy values, $\langle E_{\mathrm{ph}}^{\mathrm{E}} \rangle$, of all peaks

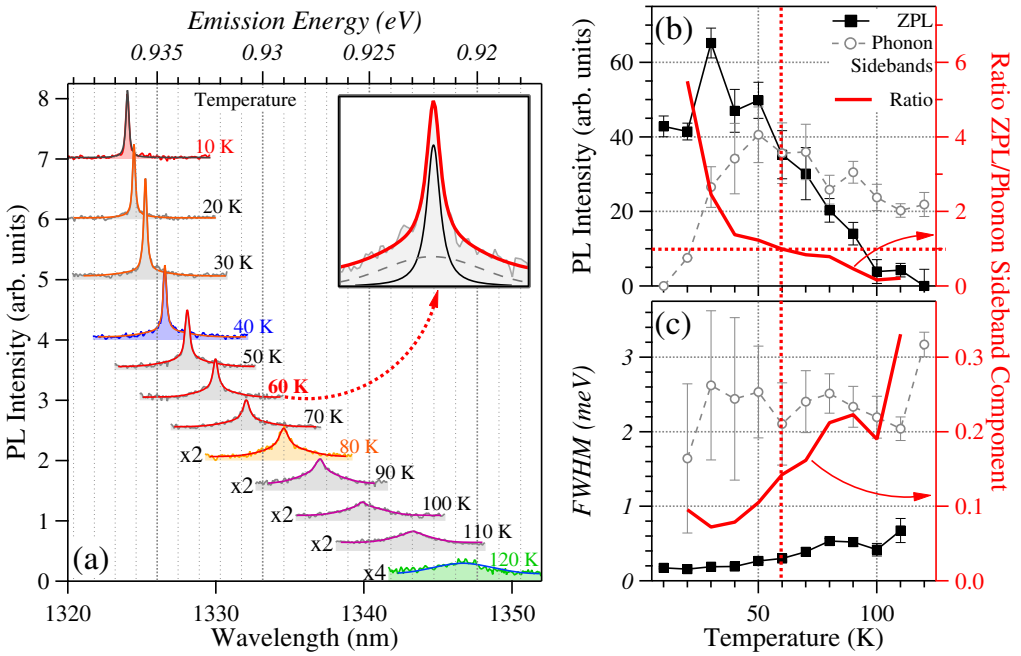

Figure 6. (a) Zoom of 'Peak 3' from figure 5 to determine the temperature-dependent line shape transition from the pure ZPL to the predominantly acoustic phonon broadened spectral appearance, applying Lorentzian and Gaussian fits, respectively. The inset presents the fit curves to the 60 K data, i.e. the total fit (thick red line), the ZPL part (solid black line) and the phonon sideband part (dashed grey line). (b) Temperature dependence of the ZPL (Lorentzian, black squares) and phonon sideband (Gaussian, grey circles) components of the integrated PL intensity and (c) the respective line width (FWHM) components; the red lines indicate the ratios of the ZPL to phonon sideband values.

are between 12 and 14 meV, which is significantly lower than the bulk LO(Γ) phonon energies of GaAs (35 meV) or InAs (29 meV), a significant contribution of acoustic phonons can be assumed (TA(X) of GaAs: 10 meV, InAs: 7 meV). The value of the coupling constant varies between $S_c = 32$ and 45 meV. The obtained result of a major contribution of the acoustic phonons is in good agreement with the afore-discussed crossover between ZPL and acoustic phonon sideband dominated PL.

Secondly, we discuss the alteration and broadening of the QD emission line width (figure 7(b)). The suggested model, again accounting for electron–phonon interaction-mediated broadening, results in another empirical fit function [31] similar to equation (2),

$$\Gamma(T) = \Gamma_0 + \frac{\Gamma_1}{\exp[\langle E_{\mathrm{ph}}^{\mathrm{B}}\rangle/(k_{\mathrm{B}}T)] - 1}, \tag{3}$$

where $\langle E_{\mathrm{ph}}^{\mathrm{B}}\rangle$ is the energy of the phonons causing the line broadening, Γ_0 is the zero-temperature line width (intrinsic broadening) and Γ_1 is the broadening constant.

The fitting of 'Peaks 1–3' for temperatures up to about 100 K reveals similar values for the phonon energies, $\langle E_{\mathrm{ph}}^{\mathrm{B}}\rangle = 22$–$32$ meV, with the average of about 27 meV, which coincides well with the bulk LO(Γ) phonon energy of InAs and which is also close to the bulk LO(Γ) phonon

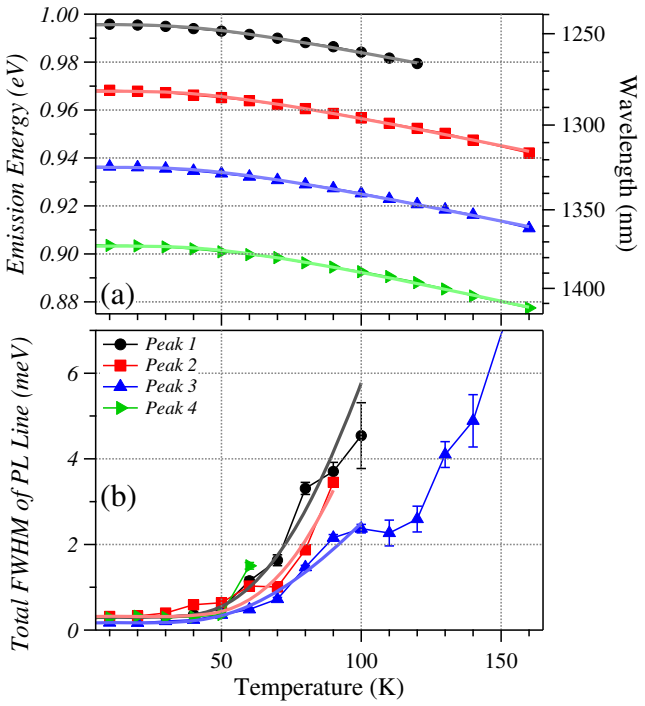

Figure 7. (a) The temperature-dependent line shifts of four selected peaks, 'Peaks 1–4', as identified in figure 5. (b) The line widths (FWHM) as a function of temperature for the same four selected peaks. All emission energy and line width values of the analysed peaks are obtained from the data displayed in figure 5. The corresponding fits to the PL energy and FWHM data, according to equations (2) and (3), are shown as solid lines. Note that the data points are only displayed in the temperature range up to the quenching of the respective peak and, for the FWHM data, until no more reliable evaluation due to peak overlap was possible.

energy of the InGaAlAs barrier [32]. (Note that reliable line width values for 'Peak 4' could not be extracted for $T \geqslant 50$ K because of the increasing overlap with a neighbouring PL line, and that the respective data were thus not considered.) The coupling constant, Γ_1, however, varies quite significantly between the peaks ($\Gamma_0 \approx 30$–160 meV) as it strongly depends on the exact environment of the respective dot, its size, potential, strain (anisotropy), local piezoelectric field, presence of defects, etc. As can be seen in figure 7(b), the line width of the peaks remains almost unchanged of the order of 0.1–0.3 meV for temperatures below $\sim$40 K and then eventually increases more significantly above $\sim$50 K.

Although such a simple discussion and fitting already gives a rather consistent description of the temperature dependence of the individual QD excitonic emission lines, it is not in complete agreement with the detailed discussion carried out above for the single recombination line, 'Peak 3', and only provides supplementary information. It mainly describes the LO-phonon-mediated pure dephasing process by inelastic electron–phonon scattering and thus the broadening of the ZPL, which is well supported by the obtained average phonon energy of 27 meV [32, 33]. However, it does not account for the acoustic phonon sidebands and other broadening mechanisms and the respective line shape transition, because the ZPL is the

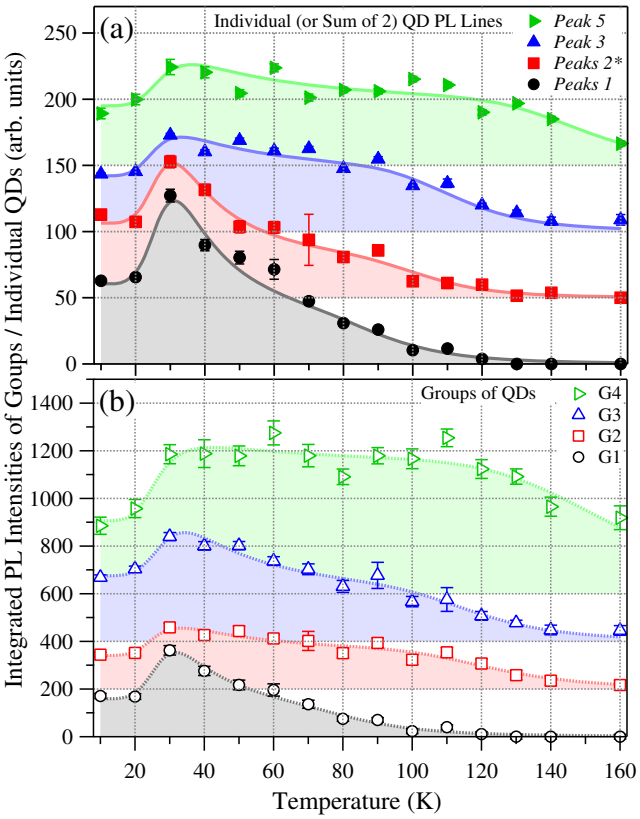

Figure 8. The PL intensity temperature dependence of (a) four individual QD peaks (or pairs) at different spectral locations and (b) the integration over the QD groups 1–4, respectively; all intensities of the analysed peaks and groups are obtained from the data displayed in figure 5. The data sets are displayed as markers (with error bars) and are fitted using equation (1); the fit results are displayed as filled curves. All data sets and corresponding fits are offset for clarity.

dominant contribution in the main part of the temperature range investigated here. It shall also be added that it was rather difficult, for this reason, to clearly obtain and assign appropriate single values for all the line widths for temperatures above ∼50 K, which is reflected by the uncertainties and deviation between data points and fit curves in figure 7(b). Besides the afore-discussed reasons, the increased broadening and intensity reduction for temperatures above 80–100 K, which can be seen in figures 6 and 7, can be due to charge fluctuations and an increased probability of various multi-phonon processes that might meet resonance conditions between QD ground and excited states or the CES, which leads to additional non-radiative decay processes of the exciton states under investigation.

3.2.2. Relative QD intensities, coupling and quenching. Figure 8 highlights the temperature dependence of the individual QD PL intensities under low-power excitation, where excited states and re-excitation processes play no major role. It displays the experimental data for individual peaks (a) and dot groups (b) (as identified in figure 5), as well as the fits to all data sets

Table 2. Fit parameters (equation (1)) for the individual QD PL lines and the energetically sorted groups of QDs; the 1σ-fit errors are omitted when of no significant magnitude ($\ll 1\%$ of the parameter value). The right column contains the optical gap energies between the InGaAlAs barrier and the respective QD/PL peak.

Type	b_1	$E^{(a1)}$ (meV)	b_2	$E^{(a2)}$ (meV)	ΔE_j (meV)
Peak 5	602 ± 8	17.0 ± 0.7	$4.3 \times 10^7 \pm 0.5 \times 10^7$	162 ± 18	≈ 322
Peak 3	985 ± 32	16.8 ± 0.2	$2.6 \times 10^7 \pm 0.2 \times 10^7$	117 ± 20	≈ 244
Peaks 2*[a]	2683 ± 254	20.7 ± 0.4	$6.3 \times 10^7 \pm 1.2 \times 10^7$	113 ± 20	≈ 218
Peaks 1[a]	3036 ± 266	21.2 ± 0.4	$9.0 \times 10^6 \pm 1.0 \times 10^6$	87 ± 8	≈ 184
Group 4	599 ± 38	15.5 ± 0.4	$2.1 \times 10^6 \pm 0.6 \times 10^6$	128 ± 32	
Group 3	809 ± 79	18.7 ± 0.5	$8.4 \times 10^6 \pm 1.5 \times 10^6$	115 ± 25	
Group 2	1010 ± 115	17.1 ± 0.5	$7.9 \times 10^6 \pm 2.4 \times 10^6$	114 ± 32	
Group 1	2665 ± 555	20.8 ± 0.8	$3.0 \times 10^6 \pm 0.7 \times 10^6$	75 ± 13	

[a]The sum of the intensities of two neighbouring peaks is considered because of their spectral overlap at higher temperatures.

using the afore-introduced equation (1), which accounts for the initial QD carrier capture and for two distinct decay processes. As a common trend of all displayed data sets, it can be observed that the lower energetic PL features persist visible in the spectra at increasing temperatures, while the higher energetic features already start to fade. The most significant fit parameters are summarized in table 2.

As already introduced before, it is assumed that the excitations (excitons/charge-carriers) are transferred to the lower-energy dots as the temperature increases; this assumption is supported by the parameters corresponding to the first escape mechanism ($i = 1$), e.g. the smaller activation energies, $E^{(a1)}$. All obtained values, for single dots and dot groups, range between 21 and 15 meV with a trend of the smaller values for the lower-energy dots. More remarkably, the corresponding coefficient, b_1, also becomes smaller with decreasing PL energy, which indicates a smaller escape probability and larger (re-)capture-rate for the lowest-energy dots and groups. This very well coincides with the carrier redistribution process from the high- to the low-energy dots as afore discussed and shown in figure 4(b).

The coefficients corresponding to the second escape mechanism (and larger activation energies), b_2, which will be discussed in more detail below, are all rather large with no clear difference between dots or groups, i.e. all such escape processes happen with much higher probabilities and are dominated by the escape—recapture is much less likely for this process.

The schematic figure 9 shall illustrate the different coupling mechanisms between dots, CES and barrier, and shall also indicate the corresponding confined discrete and continuous states as well as the assigned carrier transfer processes. The different arrows illustrate the various coupling mechanisms: (1) the inter-dot direct tunnelling (grey double-line arrow), (2) the inter-dot coupling via the CES (solid line arrows), (3) the coupling between CES and barrier (dashed line arrows) and (4) the coupling between dots and barrier (dotted line arrows). (1) is not analysed in this work and not further considered because it is a local coupling effect between two distinct dots, which could be consequently treated as a new single quantum system, a

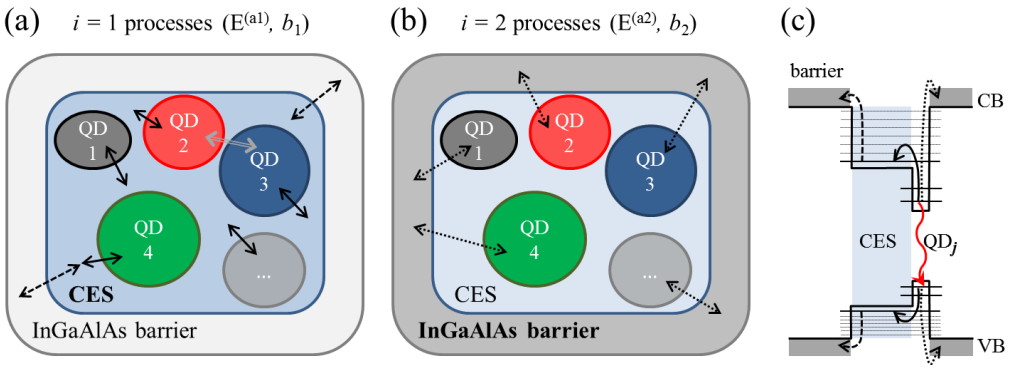

Figure 9. Schematic illustrations of the InGaAlAs barrier, the CES and some QDs inside a nano-cone, where (a) highlights the couplings related to the first carrier escape process ($i = 1$) and (b) the couplings related to the second carrier escape process ($i = 2$). (c) Illustration of a schematic simplification of the band diagram showing the assumed carrier escape, relaxation and coupling processes as well as energies for one QD and the common features CES and barrier (conduction band (CB) and valence band (VB)).

lateral QD molecule [15–17]. (2) and (3) represent the inter-dot carrier exchange via the CES and the possibility of subsequent carrier escape to the barrier (the first, $i = 1$, escape process, figure 9(a)), e.g. via phonon-assisted 'shake-up' of the carriers along the CES higher state density, as illustrated in figure 9(c). Finally, (4) represents the carrier escape from the QDs to the barrier continuum (the second, $i = 2$, escape process, figure 9(b)).

The parameters assigned to the second escape mechanism ($i = 2$), especially the larger activation energies, $E^{(a2)}$, of the individual dots (figure 8(a)) and groups of dots (b), clearly reveal this trend of decreasing activation energy with increasing QD emission energy. This trend of the fitted activation energies is comparable to the trend of the respective optical energy gaps, i.e. the energy separations between the dot PL energies and the barrier PL energy, ΔE_j, which are listed in the right column in table 2. The generally larger relative 1σ-fit errors obtained for the dot groups reflect the fact that the considered data contain PL from a certain number of individual QDs that only have the similar emission energies in common. Therefore, the fits have to account for some sort of 'averaging' of a few dots each with very similar but nevertheless slightly different values, especially with regard to the second escape mechanism.

In the following paragraph, the values obtained for this second escape process, especially the activation energies, $E^{(a2)}$, are quantitatively analysed and compared to the corresponding optical gap energies, ΔE_j. The carrier escape mechanisms from QDs can be indirectly represented by the ratio

$$\nu_j = E_j^{(a2)}/\Delta E_j, \tag{4}$$

where the index j represents a certain QD or QD group and moreover a corresponding optical gap energy (any energy difference between the described QD j and some connected higher-energy state, the InGaAlAs barrier in the present case). For a comprehensive overview, see [25].

Different carrier escape scenarios were assumed and supported by experiments [34, 35], which can be quantified as follows by using the ratio ν_j. In the case of (complete) exciton

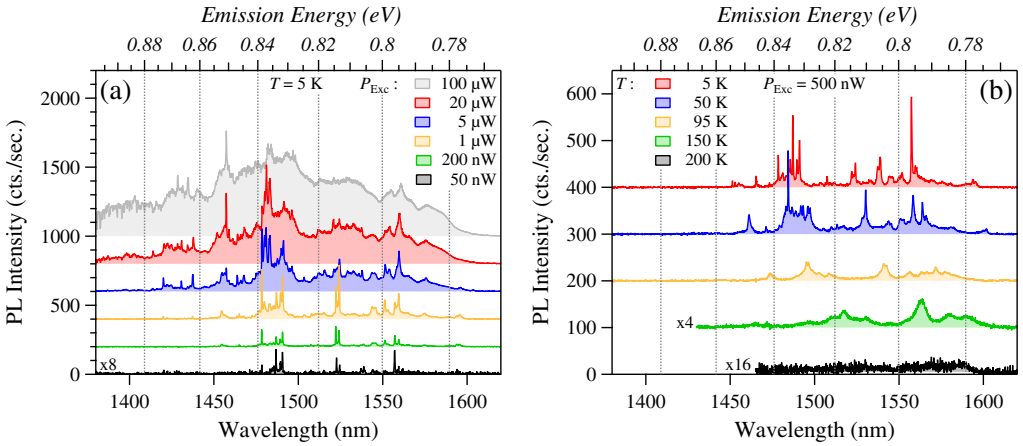

Figure 10. PL from 6 ML QDs in a $d_{QD} \approx 120$ nm Si_3N_4/Ag-embedded nanocone under non-resonant excitation. (a) Excitation power dependence at 5 K and (b) temperature dependence at 500 nW low-power excitation.

escape, the activation energy is equal to the full optical gap, i.e. $\nu_j = 1$. When in the actual escape process single carrier escape dominates, the activation energy $E_j^{(a2)}$ corresponds to the energy of the less confined carrier, i.e. $\nu_j < 1/2$. Another escape mechanism, the correlated electron–hole pair escape, has been suggested with $\nu_j = 1/2$. In this case, electrons and holes are assumed to be on average emitted as pairs, with their concentrations being equal or at least unchanged both within the dots and the barrier. This process leads to an activation energy of half the optical gap [36, 37].

In table 2, we display the fitted activation energies, $E_j^{(a2)}$, besides the corresponding optical gap energies, ΔE_j, which were obtained based on the low-temperature QD peak PL and the barrier PL shown in figure 2. Apparently, there exists a direct (linear) relation between these quantities; the fitted activation energies, $E_j^{(a2)}$, coincide well with $\Delta E_j/2$. This corresponds to $\nu_j = 1/2$ and thus clearly indicates a correlated electron–hole pair escape mechanism [23, 36, 37]. However, since $E_j^{(a2)}$ is always either $\Delta E_j/2$ or slightly on the smaller side, single carrier escape of the less confined particles, most likely holes, might also be a reasonable scenario.

4. Extension of QD luminescence to about 1.55 μm

Finally, we want to highlight the possibility that, using the same QD growth method, it is possible to not only cover photon wavelengths within the telecommunication O band, but also to reach the technologically more interesting, but more challenging, C band around 1.55 μm (0.8 eV). This is realized by increasing the nominal deposition of InAs for the QD layer from four to six MLs. Figure 10 briefly summarizes the excitation power and temperature dependence from these types of lower-energy QDs. Notably, QD emission persists up to about 150 K (or even 200 K). However, at the higher temperatures and thus longer PL wavelengths, the photon detection is limited by the cut-off of the used InGaAs detector, which is about 1.6 μm.

In comparison to the detailed presentation of the 1.3 μm QDs, similar behaviour for both the excitation and temperature dependence is found. The trend, however, suggests that the longer

wavelength 1.55 μm QD PL is indeed even more temperature stable, i.e. the corresponding activation energies might be larger. Similar inter-dot coupling as demonstrated for the 1.3 μm QDs and therefore also similar escape mechanisms are expected. A more detailed examination of the optical properties of such single QDs is currently in progress.

5. Summary and outlook

We have presented the fabrication and usage of metal-embedded nano-cones, in order to select a sub-ensemble of high-density InAs QDs emitting in the telecommunication O and C bands. Accessing such a reduced number of QDs, their electronic and optical properties could be examined in detail. Individual dot emission has been demonstrated between 1.2 and 1.6 μm (1.03–0.77 eV). The QD PL persists up to temperatures of about 150 K; the transition of the spectral properties of such individual PL lines has been analysed, accounting for the alteration of the transition energies, the line widths and shapes. The transition of a single-QD PL line from the ZPL to an acoustic sideband-dominated line shape could be demonstrated.

The PL intensity temperature dependence of both the sub-ensemble of dots in a nano-cone and individual QDs has been investigated and could be fitted with a model that includes the carrier capture and two different carrier escape processes. One of the observed escape processes could be closely connected to the inter-dot coupling of excited electronic states, which not only leads to a carrier redistribution towards the lower-energy dots but also contributes to the non-radiative carrier escape. These mechanisms are characteristic of samples with high spatial dot density, which enhances the lateral inter-dot coupling. The other observed carrier escape process is suggested to be due to correlated electron–hole pair escape and coincides well with half the optical gap energy between the InGaAlAs barrier and the respective QDs.

With this more detailed understanding of the QDs electronic properties we believe that the presented QDs, incorporated into nanometer-sized metal-embedded mesas, provide a suitable future realization of QD-based single-photon sources in the telecommunication bands. Moreover, we have shown that they have the potential for application at elevated temperatures, which well covers the liquid nitrogen temperature of 77 K, and that temperature tuning can be used to adjust the emission energy of the dots by at least 10 meV. In particularly, the dots on the low-energy side of the sub-ensemble, which is usually the one of particular interest and importance, provide the best performance with regard to temperature stability. In the future, we are planning to proceed towards the realization of single-photon and entangled photon pair sources for application in quantum information processing and quantum communication using silica-based fibre networks.

Acknowledgments

This work was partially supported by SCOPE of the Ministry of Internal Affairs and Communications, by Grant-in-Aid for Scientific Research (A) no. 21246048 and by HINTS from the Ministry of Education, Culture, Sports, Science and Technology (MEXT), Japan. CH acknowledges the Japan Society for the Promotion of Science (JSPS) for providing financial support in the form of a JSPS Fellowship for Foreign Researchers; NAJ acknowledges financial support via a MEXT scholarship.

References

[1] Michler P, Kiraz A, Becher C, Schoenfeld W V, Petroff P M, Zhang L D, Hu E and Imamoglu A 2000 *Science* **290** 2282

[2] Yuan Z, Kardynal B E, Stevenson R M, Shields A J, Lobo C J, Cooper K, Beattie N S, Ritchie D A and Pepper M 2002 *Science* **295** 102

[3] Santori C, Fattal D, Vuckovic J, Solomon G S and Yamamoto Y 2002 *Nature* **419** 594

[4] Gisin B, Ribordy G, Tittel W and Zbinden H 2002 *Rev. Mod. Phys.* **74** 145

[5] Friedler I, Sauvan C, Hugonin J P, Lalanne P, Claudon J and Gérard J M 2009 *Opt. Express* **17** 2095

[6] Akopian N, Lindner N H, Poem E, Berlatzky Y, Avron J, Gershoni D, Gerardot B D and Petroff P M 2006 *Phys. Rev. Lett.* **96** 130501

[7] Young R J, Stevenson R M, Atkinson P, Cooper K, Ritchie D A and Shields A J 2006 *New J. Phys.* **8** 29

[8] Hafenbrak R, Ulrich S M, Michler P, Wang L, Rastelli A and Schmidt O G 2007 *New J. Phys.* **9** 315

[9] Waks E, Inoue K, Santori C, Fattal D, Vuckovic J, Solomon G S and Yamamoto Y 2002 *Nature* **420** 762

[10] Loss D and DiVincenzo D P 1998 *Phys. Rev.* A **57** 120

[11] Zhou X L, Chen Y H, Liu J Q, Jia C H, Zhou G Y, Ye X L, Xu Bo and Wang Z G 2010 *J. Phys. D: Appl. Phys.* **43** 295401

[12] Krenner H J, Sabathil M, Clark E C, Kress A, Schuh D, Bichler M, Abstreiter G and Finley J J 2005 *Phys. Rev. Lett.* **94** 057402

[13] Ortner G, Bayer M, Lyanda-Geller Y, Reinecke T L, Kress A, Reithmaier J P and Forchel A 2005 *Phys. Rev. Lett.* **94** 157401

[14] Stinaff E A, Scheibner M, Bracker A S, Ponomarev I V, Korenev V L, Ware M E, Doty M F, Reinecke T L and Gammon D 2006 *Science* **311** 636

[15] Beirne G J, Hermannstädter C, Wang L, Rastelli A, Schmidt O G and Michler P 2006 *Phys. Rev. Lett.* **96** 137401

[16] Peng J, Hermannstädter C, Witzany M, Heldmaier M, Wang L, Kiravittaya S, Rastelli A, Schmidt O G, Michler P and Bester G 2010 *Phys. Rev.* B **81** 205315

[17] Hermannstädter C, Beirne G J, Witzany M, Heldmaier M, Peng J, Bester G, Wang L, Rastelli A, Schmidt O G and Michler P 2010 *Phys. Rev.* B **82** 085309

[18] Robledo L, Elzerman J, Jundt G, Atatüre M, Högele A, Fält S and Imamoglu A 2008 *Science* **320** 772

[19] Kim D, Carter S G, Greilich A, Bracker A S and Gammon D 2011 *Nat. Phys.* **7** 223

[20] Takemoto K, Takatsu M, Hirose S, Yokoyama N, Sakuma Y, Usuki T, Miyazawa T and Arakawa Y 2007 *J. Appl. Phys.* **101** 081720

[21] Akahane K, Yamamoto N, Ohtani N, Okada Y and Kawabe M 2003 *J. Cryst. Growth* **256** 7

[22] Akahane K, Yamamoto N and Kawanishi T 2011 *Phys. Status Solidi* a **208** 425

[23] Jahan N A, Hermannstädter C, Huh J-H, Sasakura H, Rotter T J, Ahiwar P, Balakrishnan G, Akahane K, Sasaki M, Kumano H and Suemane I 2012 submitted arXiv:1202.1360

[24] Huh J-H, Hermannstädter C, Akahane K, Sasakura H, Jahan N A, Sasaki M and Suemune I 2011 *Jpn. J. Appl. Phys.* **50** 06GG02

[25] Gélinas G, Lanacer A, Leonelli R, Masut R A and Poole P J 2010 *Phys. Rev.* B **81** 235426

[26] Le Ru E C, Fack J and Murray R 2003 *Phys. Rev.* B **67** 245318

[27] He J, Krenner H J, Pryor C, Zhang J P, Wu Y, Allen D G, Morris C M, Sherwin M S and Petroff P M 2007 *Nano Lett.* **7** 802

[28] Krenner H J and Petroff P M 2009 *Solid State Commun.* **149** 1386

[29] Völk S, Schülein F J R, Knall F, Reuter D, Wieck A D, Truong T A, Kim H, Petroff P M, Wixforth A and Krenner H J 2010 *Nano Lett.* **10** 3399

[30] Arians R, Kümmell T, Bacher G, Gust A, Kruse C and Hommel D 2007 *Appl. Phys. Lett.* **90** 101114

[31] Cingolani R, Lomascolo M, Rinaldi R, Spagnolo V, Scamarcio G, Ferrara M, Hase A and Künzel H 1992 *Solid State Commun.* **84** 679

[32] Borri P, Langbein W, Woggon U, Stavarache V, Reuter D and Wieck A D 2005 *Phys. Rev.* B **71** 115328
[33] Sanguinetti S, Poliani E, Bonfanti M, Guzzi M, Grilli E, Gurioli M and Koguchi N 2006 *Phys. Rev.* B **73** 125342
[34] Sanguinetti S, Colombo D, Guzzi M, Grilli E, Gurioli M, Seravalli L, Frigeri P and Franchi S 2006 *Phys. Rev.* B **74** 205302
[35] Schulz W-M, Roßbach R, Reischle M, Beirne G J, Bommer M, Jetter M and Michler P 2009 *Phys. Rev.* B **79** 035329
[36] Michler P, Hangleiter A, Moser M, Geiger M and Scholz F 1992 *Phys. Rev.* B **46** 7280
[37] Yang W, Lowe-Webb R R, Lee H and Sercel P C 1997 *Phys. Rev.* B **56** 13314